nature nanotechnology

ARTICLES

PUBLISHED ONLINE: 28 NOVEMBER 2016 | DOI: 10.1038/NNANO.2016.254

Observation of extreme phase transition temperatures of water confined inside isolated carbon nanotubes

Kumar Varoon Agrawal†, Steven Shimizu†, Lee W. Drahushuk, Daniel Kilcoyne and Michael S. Strano*

Fluid phase transitions inside single, isolated carbon nanotubes are predicted to deviate substantially from classical thermodynamics. This behaviour enables the study of ice nanotubes and the exploration of their potential applications. Here we report measurements of the phase boundaries of water confined within six isolated carbon nanotubes of different diameters (1.05, 1.06, 1.15, 1.24, 1.44 and 1.52 nm) using Raman spectroscopy. The results reveal an exquisite sensitivity to diameter and substantially larger temperature elevations of the freezing transition (by as much as 100 °C) than have been theoretically predicted. Dynamic water filling and reversible freezing transitions were marked by 2–5 cm^{-1} shifts in the radial breathing mode frequency, revealing reversible melting bracketed to 105–151 °C and 87–117 °C for 1.05 and 1.06 nm single-walled carbon nanotubes, respectively. Near-ambient phase changes were observed for 1.44 and 1.52 nm nanotubes, bracketed between 15–49 °C and 3–30 °C, respectively, whereas the depression of the freezing point was observed for the 1.15 nm nanotube between −35 and 10 °C. We also find that the interior aqueous phase reversibly decreases the axial thermal conductivity of the nanotube by as much as 500%, allowing digital control of the heat flux.

When water[1] is confined to nanometre-sized pores, such as the interior of a carbon nanotube (CNT)[2], it exhibits unusual phase behaviour due to confinement effects[3–8]. Specifically, the intermolecular potential of the container wall can exert the equivalent of an additive or subtractive pressure on the fluid, shifting the phase boundary. Below a critical confinement length scale (approximately 2.5 nm), the theory on depression of the freezing point of water, which is described by the continuum thermodynamics and the Gibbs–Thomson effect[9,10], breaks down. However, phase transitions within single, isolated pores of known diameter have not yet been measured to quantify the extent of deviations from the classical thermodynamics. When confined inside sub-1.5 nm diameter CNTs, water can freeze to form ice NTs[3,11–24], which are of fundamental scientific interest, and attractive as potential nanoscale ferroelectric devices[18,22], gas nanovalves[19], nanoscale flow sensors[25] and high-flux membranes[7,26–29]. Moreover, molecular simulations predict that confined water in CNT can freeze above 0 °C[12,15], approaching room temperature, making hydrated CNTs a possible candidate for a latent heat thermal storage system[30]. This is supported by experimental evidence, but the specific diameters required for the design of such systems have not been demonstrated. Generally, the understanding of fluid phase transitions inside CNTs has been limited to reports that are based on molecular dynamics (MD) simulations[3,12,15,17,18,23] and experiments on polydisperse powders and suspensions of CNTs[11,15,17,21]. Typically, MD simulations are subjected to the limitations of forcefield accuracy[23,31,32]. On the other hand, experiments on polydisperse CNTs greatly reduce the resolution of the diameter-dependent behaviour of confined water. Recent simulations[23] that investigate the forces that drive the aqueous filling of the narrowest of CNT diameters find different mechanisms depending on the diameter range. Water in 0.8–1.0 nm CNT pores has been shown to exist in a vapour-like, entropically stabilized state[23]. Interestingly, simulations predict that between 1.1 and 1.2 nm, stabilization becomes enthalpic with an ice-like phase, followed by a bulk-like liquid phase stabilization for tubes larger than 1.4 nm in diameter. Here we use two different techniques to explore the diameter-dependent phase boundaries of ice NTs formed within isolated CNTs over a range of diameters from 1.05 to 1.52 nm (chiralities in Supplementary Tables 1 and 2). We show that the phase behaviour of water inside the single-walled and double-walled nanotubes (SWNTs and DWNTs, respectively) can be monitored using the dynamic shift in the frequency of the Raman radial breathing mode (RBM). This feature to is used to study fluid phase filling and reversible freezing transitions at temperatures higher than 100 °C. Our study demonstrates that the phase transitions of confined water in CNTs are extremely diameter-dependent, and freezing transitions as high as 138 °C for 1.05 nm metallic SWNTs were observed, close to the range of enthalpy stabilized, ice-like water as predicted[23]. We then utilize a laser-heating model to show that aqueous filling of the CNT substantially reduces the axial thermal conductivity (k_a), providing a means of reversibly switching the heat flux in the conduit.

Water filling indicated by upshift in RBM frequency

The experiments utilize single, isolated chemical vapour deposition (CVD)-grown SWNTs and DWNTs using a modification of the platform that we reported previously for ion-transport[26,33,34]. Briefly, we synthesized centimetre-long horizontally aligned CNTs by CVD of methane on an Si wafer containing a thin strip of the Fe catalyst on its edge (Fig. 1a,(i)–(ii)). Post-CVD, the tube ends were cut opened by air plasma, over which two polydimethysiloxane (PDMS) reservoirs were deposited to facilitate water infiltration (Fig. 1a,(iii)–(vi)). Following this, individual CNTs on the platform

Department of Chemical Engineering, Massachusetts Institute of Technology, Cambridge, Massachusetts 02139, USA. †These authors contributed equally to this work. *e-mail: strano@mit.edu

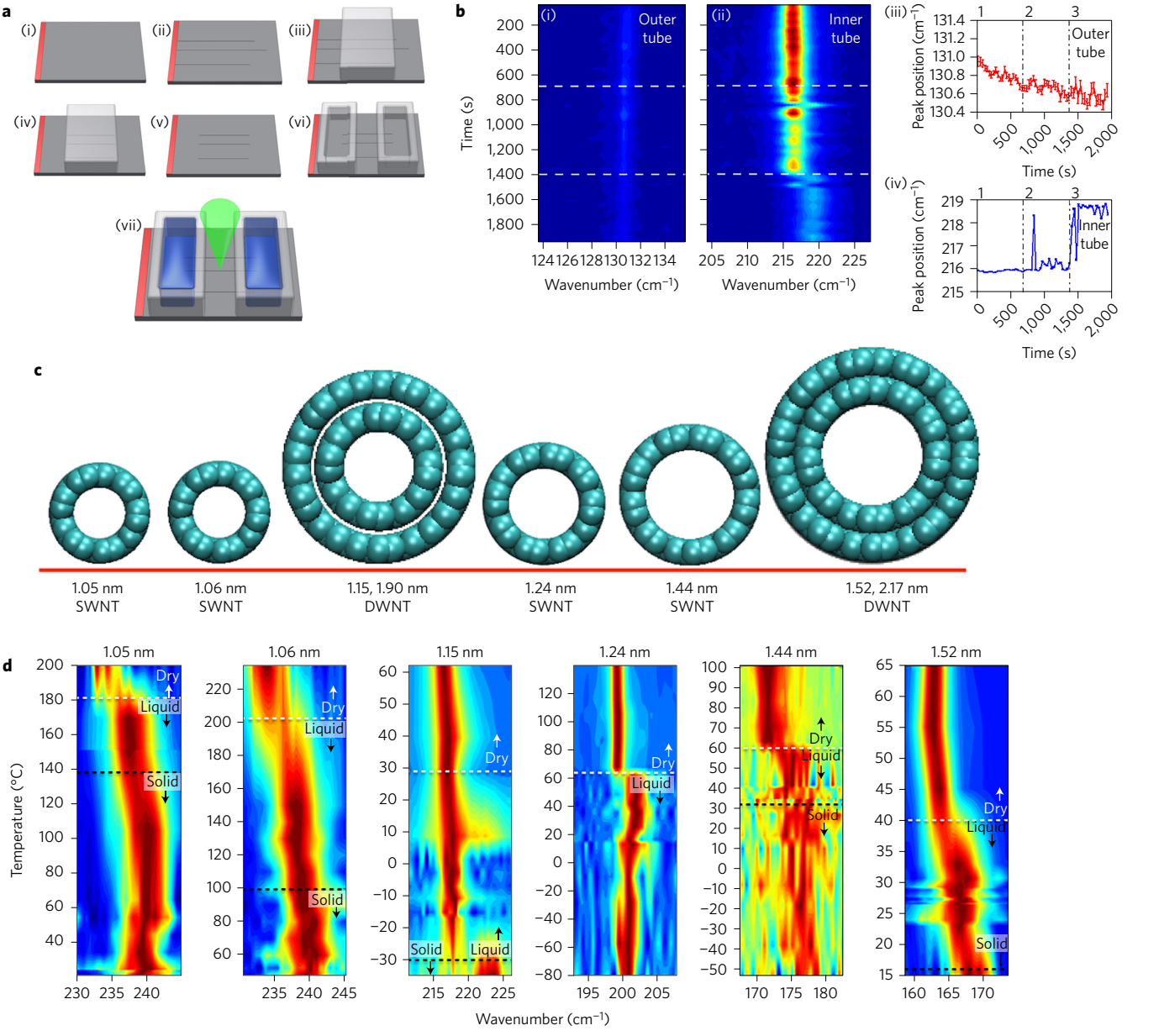

Figure 1 | Evidence of filling and phase transition of water inside CNTs. a, Fabrication of the platform, which comprises isolated CNTs connected to two reservoirs. (i) A catalyst solution consisting of iron nanoparticles (red) is deposited along an edge of the Si substrate. (ii) Centimere-long, horizontally aligned CNTs are grown using CVD with methane. (iii) A PDMS protective mask is placed on the middle section of the CNTs. (iv) Air plasma removes the uncovered parts of the CNTs, opening up the ends. (v) The PDMS mask is removed. (vi) Two PDMS reservoirs are adhered to the surface. (vii) The reservoirs are filled with water and microRaman spectroscopy is performed on the CNT. **b**, Temporal study of the RBM frequency. (i,ii) A time-map showing the evolution of RBM frequency and intensities for the 1.15 nm DWNT. Dotted lines indicate the time points at which water is added to the reservoirs. (iii,iv) Fitted peak positions for the outer and inner RBMs, respectively. 1, reservoirs empty; 2, water added to right reservoir; 3, water added to left reservoir. **c**, A visual MD model of the CNTs studied here. The 1.06 nm SWNT was bundled with a 1.55 nm SWNT. **d**, A contour plot of the representative RBM frequency (based on the signal-to-noise ratio) versus temperature for the six tubes studied here. The white line represents the transition from the dry to the water-filled state, whereas the black line signifies the freezing transition of the confined water.

were probed by microRaman spectroscopy for the determination of the CNT diameter and metallicity using the RBM[35] and shape of the *G* peak[36], respectively (Fig. 1a, vii, details in Supplementary Section 1). The RBM and *G* peaks are radial and tangential vibrational modes, respectively. We calculated the inner diameters of the CNTs using the function d (nm) = 248/RBM (cm^{-1}), which has been shown to accurately predict diameter of Si-supported isolated SWNTs and DWNTs with errors less than 5%[35,37]. On filling both of the reservoirs with water, thereby contacting bulk water with the open tube ends, we observe an upshift in the RBM frequency, consistent with the infiltration of water inside the nanotube (Fig. 1b). In the case of the DWNTs, while the RBM of the inner tube underwent a blue shift, that of the outer tube did not change, consistent with interior filling. The water velocity based on the temporal shift of the RBM frequency was 18 μm s^{-1}, in rough agreement with a calculated flow (13 μm s^{-1}) based on a no-slip Hagen–Poiseuille model and the estimated Laplace pressure (Supplementary Section 2). On the basis of these observations, we therefore assign this Raman shift to a liquid water phase that fills the nanotube as the open ends contact bulk water in the reservoir. This is consistent

with literature observations, where an RBM upshift of 1.5–3.5 cm^{-1} has been reported on water filling[38,39]. Moreover, a 2–6 cm^{-1} RBM upshift was predicted for water filling inside a (22,0) SWNT in MD simulations[40]. We did not observe RBM shifts for unopened tubes in the presence of water (Supplementary Fig. 1). Also, the RBM did not change on heating to up to 200 °C (Supplementary Fig. 2), ruling out any RBM shift due to external physisorbed water.

Isolated CNTs filled with water provide a unique opportunity to study the phase behaviour within a singular diameter for the first time. To study the temperature dependence of the water phase, we varied the temperature of the CNT by two orthogonal methods. In method 1 we used a temperature-controlled stage, changing the temperature of the entire platform during spectroscopy. In method 2, the incident laser (8 mW, 2.33 eV) was attenuated using a variable neutral density (ND) filter to control the temperature of the 5 μm spot on the CNT while the stage temperature was kept isothermal[41]. A combination of these two methods was used to attain the desired temperature. The local temperature was calibrated by the *G*+ peak shift, which varies linearly with the temperature of the CNT[41–43]. The CNT temperature for method 2 was calculated as:

$$T = T_{\text{stage}} + \frac{\beta}{X} P_{\text{laser}} \quad (1)$$

where

$$X = \left(\frac{\partial G}{\partial T}\right)_{P_{\text{laser}} \approx 0} \quad \text{and} \quad \beta = \left(\frac{\partial G}{\partial P_{\text{laser}}}\right)_{T=20^{\circ}\text{C}}$$

where T_{stage} and T are temperatures of the stage and the CNT, respectively; P_{laser} is the Raman laser power. The SWNTs and DWNTs studied in this work are depicted in Fig. 1c. A complete data set for RBM frequency as a function of temperature for the six CNTs is provided in Supplementary Fig. 3. All subsequent analysis of the phase transition temperature used the entire data set. For each spectrum, the background was subtracted and RBM peaks were fit using a three parameter Lorentzian using MATLAB's lsqnonlin. RBM peak positions that were recorded at the same temperature, in the same heating/cooling cycle and with poor signal-to-noise ratios were averaged. Maps of representative RBM frequencies as a function of temperature are shown in Fig. 1d, revealing up to two distinct, reversible transitions per CNT. The first transition (white line, Fig. 1d) has already been assigned to the presence of a liquid water phase. The second transition, invariably at lower temperature (black line, Fig. 1d) is consistent with the formation of a solid phase of water, as analysed below.

Freezing transition indicated by a second RBM upshift

A histogram of RBM frequencies (all data in Supplementary Fig. 3) indicates up to three distinct states (Fig. 2a–c). The lowest frequency RBM position relates to the dry-state, corresponding to minimally or vapour filled CNTs (pink bracket, Fig. 2b), whereas the middle peak in the histogram is assigned to liquid water (green bracket, Fig. 2b) from the dynamic filling experiments (Fig. 1b). The third histogram peak, which appears at lower temperatures, is assigned to a liquid–solid or freezing transition (cyan bracket, Fig. 2b). This transition invariably causes a shift of the RBM to a higher frequency consistent with the formation of a phase with a higher elastic modulus. Specifically, we calculated the RBM shift of water-filled CNTs using the simplified Flügge equation[44]. The CNT and internal water can be modelled as two coaxial, elastic shells interacting via a van der Waals potential, with atoms in both shells oscillating with temporal displacements $w_c(t)$ and $w_w(t)$ from their mean positions for carbon and water shells respectively (equations (2) and (3)).

$$\frac{w_c(t)}{R_c^2} + \frac{(\rho h)_c}{(Eh)_c}(1-\upsilon_c^2)\frac{\partial^2 w_c(t)}{\partial t^2} = \frac{1}{(Eh)_c}(1-\upsilon_c^2)P_c \quad (2)$$

$$\frac{w_w(t)}{R_w^2} + \frac{(\rho h)_w}{(Eh)_w}(1-\upsilon_w^2)\frac{\partial^2 w_w(t)}{\partial t^2} = \frac{1}{(Eh)_w}(1-\upsilon_w^2)P_w \quad (3)$$

$$P_c = \frac{cR_c}{R_w}(w_c - w_w),\ P_w = c(w_w - w_c)$$

where Eh and ρh are in-plane stiffness and mass density per unit lateral area of the shells, respectively, υ is Poisson's ratio, P is the net radial pressure exerted on the shells, c is the van der Waals interaction coefficient between carbon and water shells and h is thickness of carbon shell. Equations (2) and (3) predict an in-phase RBM shift to higher frequency on increasing the elastic modulus of the enclosed water (Supplementary Section 3), consistent with this assignment to a liquid–solid phase transition. Such solid interior phases, and their remarkable appearance at highly elevated temperatures, allow the study of ice NTs at elevated temperatures, and highlight useful applications that can be exploited at room temperature and above.

An analysis of the phase transition temperature was carried out using the entire RBM data set (Supplementary Fig. 3). RBM peaks with a notable shoulder were deconvoluted to two peaks (liquid and vapour, solid and liquid), and are represented in Fig. 2b by circular markers with a size proportional to the peak area. Estimates of the phase transition temperatures were made using a finite-width Heaviside fitting algorithm (equation (4), Methods) and the results are shown in Fig. 2b. Confidence intervals in the fitting were calculated by the bootstrap resampling method[45]. The freezing transition for water confined in the 1.05 and the 1.06 nm SWNTs occurred at extremely high temperatures (105–151 °C and 87–117 °C, respectively), whereas water in the 1.44 nm SWNT, and in the 1.15 and 1.52 nm DWNTs froze in the temperature range of 15–49 °C, −35 to 10 °C and 3–30 °C, respectively (Fig. 2b,(i)–(iii) and (v)–(vi), Supplementary Figs 4–6, 9 and 10 and Supplementary Table 3). The presence of a superheated solid phase can be discounted since freezing at these high temperatures was also observed during cooling cycles. Hysteresis is observed for only one diameter (1.06 nm SWNT, Fig. 2b,(ii), Supplementary Fig. 5), where melting occurred at a higher temperature than freezing. We did not observe a freezing transition for the 1.24 nm SWNT on cooling down to −80 °C, the limit of our experimental technique due to frost formation (Fig. 2b,(iv) and Supplementary Fig. 7). Although water desorption was observed from the 1.15, 1.24, 1.44 and 1.52 nm CNTs at temperatures below the boiling point of bulk water (also reported for 1.17 nm suspended SWNTs by photoluminescence studies[46]), for water filled 1.05 and 1.06 nm tubes, the dry states were only restored by heating the tubes to 171 and 199 °C, respectively (Supplementary Table 3).

We did not observe a significant RBM shift for unopened tubes on changing the temperature (Supplementary Fig. 2), confirming that RBM shifts for etched tubes on exposure to water is indication of phase-transition events (filling and freezing transitions). The RBM upshifts corresponding to phase transitions were nonlinear (Supplementary Fig. 10 and Supplementary Table 4), unlike the linear shifts in the *G*+ peak position[41–43]. On freezing, decreasing the CNT temperature did not yield additional upshifts in the RBM peak position (Fig. 3a,(i)). Moreover, the RBM shifts were completely reversible. Oscillating the temperature of the water filled CNTs by method 1 (Fig. 3a,(i)) or by method 2 (Fig. 3a,(ii)) correspondingly oscillated the RBM peak position. These reversible RBM shifts in 5 μm domains of the CNT support the conclusion that the frozen water is not superheated ice, but instead is a

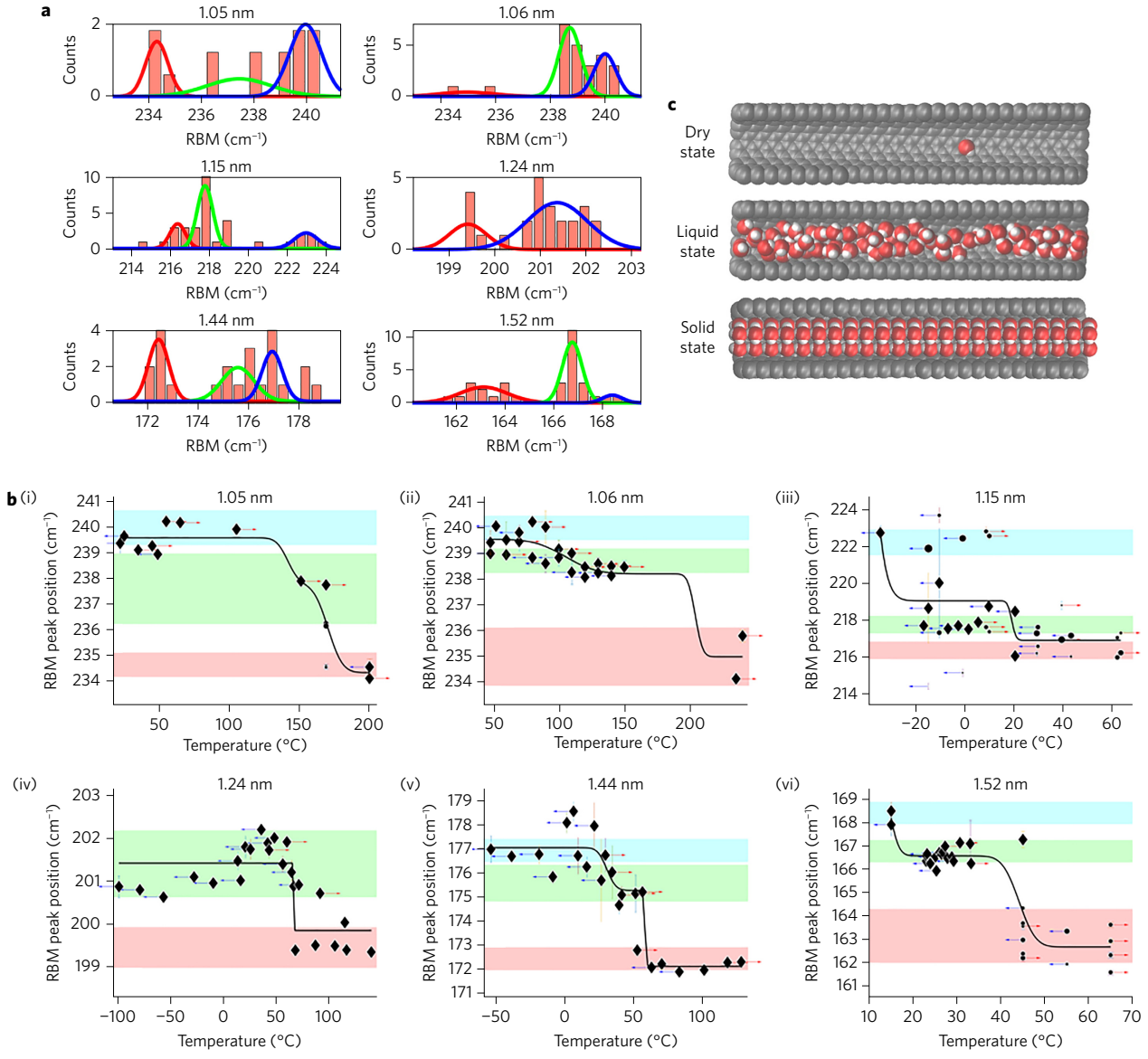

Figure 2 | Diameter-dependent vapour–liquid and liquid–solid phase transitions of confined water inside CNTs. a, Histograms of the RBM peak positions for the six CNTs. Gaussian peaks are fitted to the histogram data, showing up to three peaks that correspond to the distinct states of the CNTs. **b**, RBM peak position as a function of tube temperature. A combination of method 1 and method 2 was used to achieve the temperature. Blue left-pointing arrows indicate cooling cycles; red right-pointing arrows indicate heating cycles; the lack of arrows indicates a neutral, starting state. In the case of an RBM peak with a shoulder, we deconvoluted the peaks and the resulting data points are plotted using circular markers with a size that is proportional to the peak area. Single-peak RBMs are represented by the diamond markers. The fitting for deconvoluted data points included weights proportional to the peak area. The shaded brackets correspond to the three states of the CNTs (cyan, solid water; green, liquid water and pink, dry CNTs). The width of each bracket is the FWHM of the peaks fitted to the RBM histogram in **a**. The black curves are finite-width Heaviside fits (confidence interval in Supplementary Table 3) and comparative linear fits are shown in Supplementary Fig. 10 and Supplementary Table 4. The RBM error bars originate from the error in fitting the RBM peak with a Lorentzian curve. **c**, Illustration of the three CNT states.

stable thermodynamic state. Moreover, the two heating methods used here led to consistent phase transition data (Fig. 3b).

Extreme freezing transitions inside of CNTs

Next, we compare our result with those in the literature in a plot of freezing transition versus nanotube diameter (Fig. 4a). Freezing transitions of water inside larger-diameter multi-walled NTs[47] (>2 nm) follow the Gibbs–Thompson equation[9,10], and are inversely proportional to diameter. In contrast, a significant diameter dependence is observed with the SWNTs and DWNTs studied in this work (diameters <1.60 nm). Freezing transitions for two isolated SWNTs (1.05 and 1.06 nm) significantly exceed the predictions of MD simulations that show elevations of 17 °C for 1.08 nm SWNTs[12]. In our previous work on SWNT diameter-dependent ion transport[34], we note that we did not observe K^+ ion conductance at 25 °C through CNTs in this diameter range, which would be solid ice according to the measurements in this work, but did so for smaller (0.9 nm) and larger (1.2 nm) tubes. Also, averaging the freezing points for 1.05, 1.06 and 1.15 nm isolated CNTs yields a value that agrees with the XRD study of 1.17 ± 0.11 nm SWNT bundles[15], where polydispersity could average the observed transitions. Continuous freezing transitions for CNTs smaller than 1.2 nm in were observed in MD simulations[12], whereas larger tubes showed first-order freezing transitions of water.

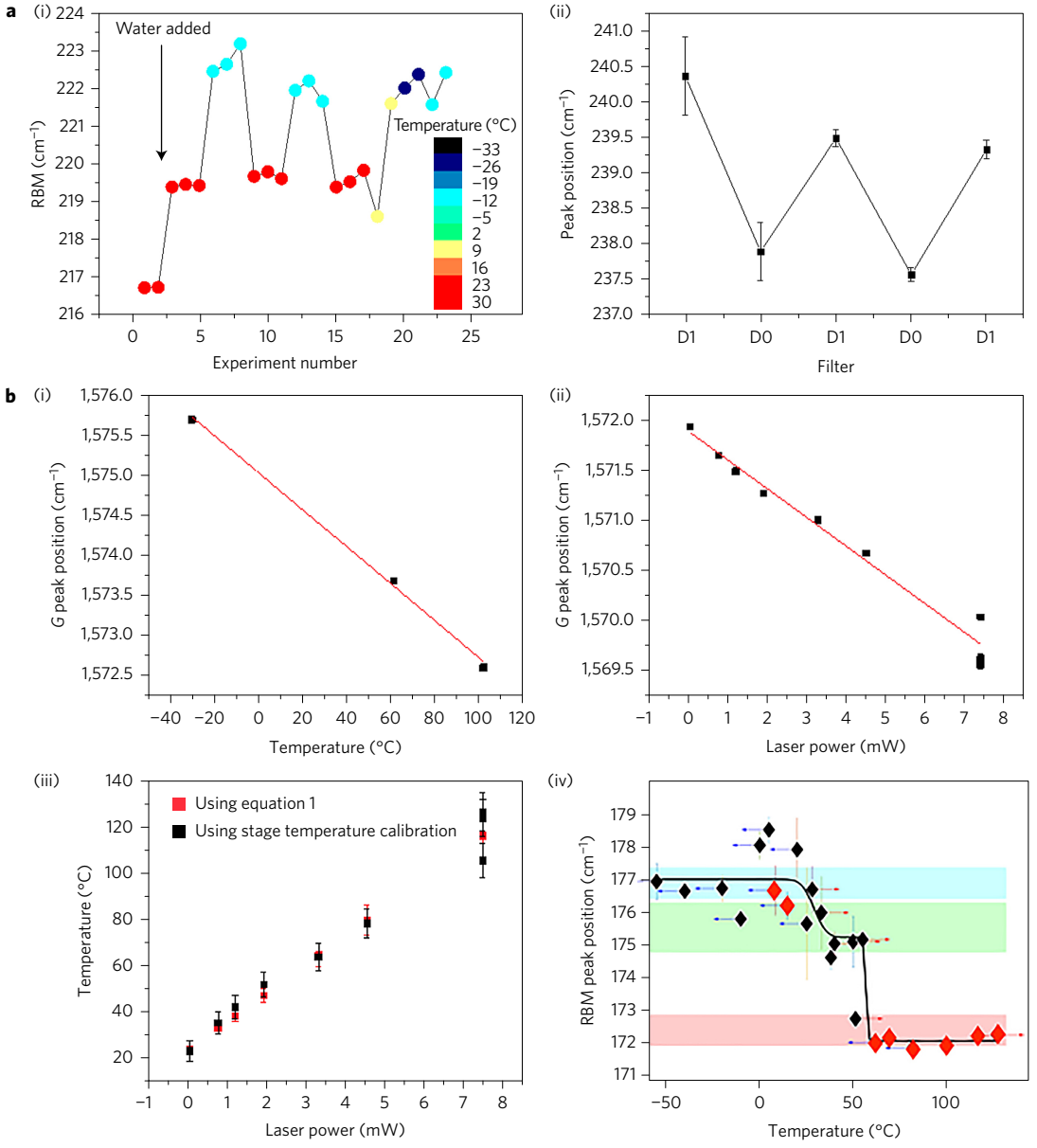

Figure 3 | Reversibility of the water phases inside the CNT on heating and cooling, and agreement in the phase transition data obtained by the two heating methods. a, RBM frequency of the CNTs as a function of heating and cooling oscillations. (i) The temperature of the 1.15 nm CNT was varied by method 1, changing the stage temperature. (ii) The temperature of the 1.06 nm CNT was varied by method 2, changing laser intensity between the low power 0.8 mW (D1) and the high power 8 mW (D0) modes. The error bars for the peak positions are the errors in fitting them with a Lorentzian curve. **b**, (i) Calibration of the *G* peak position with the stage temperature. (ii) Change in the *G* peak position as a function of the laser power. (iii) Agreement between temperature calculated by equation (1) and that calculated using the *G* peak position calibration. The error bars in temperature are errors propagated from errors in χ and β (Supplementary Tables 6 and 7). (iv) A good agreement is found within the phase transition data generated by the two distinct heating methods for a 1.44 nm CNT. Here data highlighted by the black markers refer to method 1 (stage heating) and the red markers refer to method 2 (laser heating). The error bars originate from the errors in fitting the RBM peak positions.

Our experimental results for the 1.06 nm SWNT seem to agree with this continuous freezing transition. For a 1.24 nm diameter CNT, we did not observe a freezing transition, although water filled this tube below 66 °C. We hypothesize that the freezing transition temperature for this tube could be below the cooling limit of our set-up (−80 °C), and suppressions of this magnitude are predicted for CNTs in this range by MD simulations[12]. For our larger-diameter CNTs, 1.44 and 1.52 nm, we observe a freezing point elevation of a modest extent at 31 and 15 °C, respectively, also of the order predicted by MD. This transition temperature approaches ambient temperature, highlighting that this diameter can be applied to new phase-change insulators for thermal storage systems[30].

These extreme phase transitions for a narrow range of diameters of 1.05 and 1.06 nm CNTs appear to be consistent with previous studies[12,15,23] that found an ice-like single-layer polygonal nanotube phase that is stabilized by a strong hydrogen-bonded network. Close to this narrow range (1.1 and 1.2 nm), interior water is reported to have a higher number of rigid hydrogen bonds per molecule (HBM) than that in bulk water (3.6 compared to 3.5 HBM in bulk), leading to a net decrease in enthalpy compared to bulk[23]. Hence, in this regime, this ice-like phase should be significantly more stable, consistent with our observations. The increased HBM is apparently unique to this narrow range (among those studied between 0.8–2.7 nm CNTs), and is

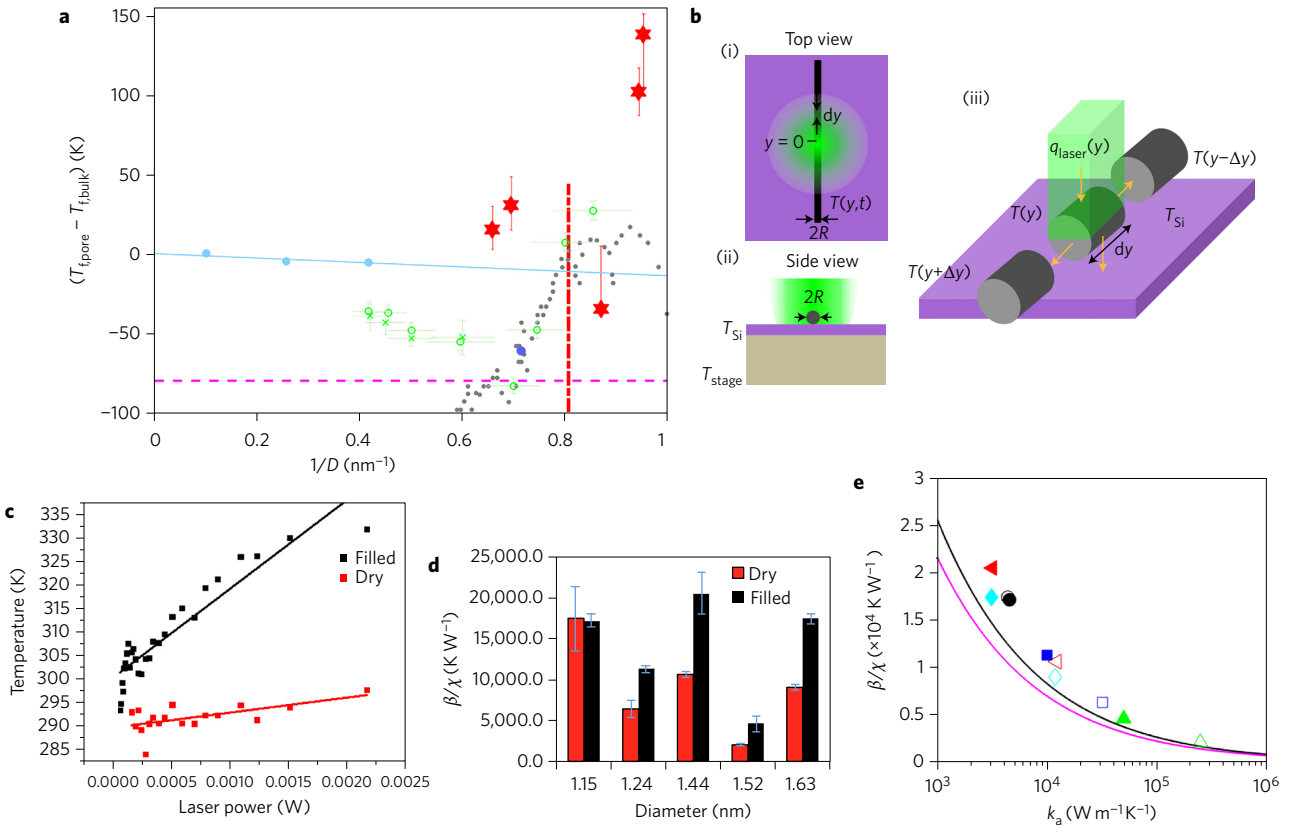

Figure 4 | Comparison of the diameter-dependent phase transition temperatures and reduction in the axial conductivity of the CNTs on water filling. **a**, A global plot for the freezing point depressions of water confined in CNTs. Red markers indicate experimental data from this work. The error bars in these data originate from the uncertainty in Heaviside fittings in Fig. 2b. The dashed red vertical line represents the 1.24 nm SWNT for which no freezing transition was observed. The dashed magenta horizontal line is the lower temperature bound for the experiment (−80 °C). Cyan markers indicate experimental freezing point depressions for water inside larger MWNTs[47]. The fitted cyan line is the expected trend for freezing point depression as per the Gibbs–Thomson effect. Grey markers indicate the results from the MD simulations on freezing transition of water inside SWNT[12]. The green and blue markers are experimental (XRD and NMR) measurements on polydisperse SWNT powders and suspensions[15,21]. **b**, A schematic for laser heating CNTs on a silicon substrate. (i) A laser is focused on a spot along the length of the tube. This position is defined to be $y = 0$ in the model. (ii) The Si substrate in the experiment is placed on top of a silver heating block. The temperature of the Si substrate, T_{Si}, is assumed to be the same as that of the stage, T_{stage}. (iii) The energy balance for a differential element of the CNT. Heat from the laser beam, q_{laser}, is dissipated to the colder regions of the CNT, and to the underlying silicon substrate. **c**, Local temperature of the 1.24 nm CNT versus the laser power in the filled and dry states. **d**, Comparison of β/χ for CNTs in the filled versus dry states. The data used for the plot are provided as Supplementary Tables 6 and 7. The error bars in β/χ originate from the errors in estimating χ and β (Supplementary Tables 6 and 7). **e**, A plot of β/χ versus k_a showing that on filling, CNTs undergo decrease in k_a. The black and the pink curves are obtained from the laser heating model (Supplementary equation (16)) for tubes of 1.15 and 1.63 nm in diameter, respectively. The black, blue, red, green and cyan symbols represent 1.15, 1.24, 1.44, 1.52 and 1.63 nm diameter tubes, respectively. Open symbols represent tubes in the dry state, whereas solid symbols represent tubes in the filled state.

attributable to pentagonal and hexagonal ice NTs. Our findings are also consistent with the theory[48] that the magnitude and sign of freezing point deviation depends on the reduced pore width and the ratio of fluid-wall to fluid-fluid interactions (α). We suggest that the density and relative interactions of water (water–carbon and water–water), which determine α, would also be a strong function of diameter.

The platform also allowed us to compare the relative thermal conductivity in the dry or vapour-filled CNTs versus the liquid-filled states. A liquid-filled tube displays a greater temperature rise for a given laser power compared with the vapour or dry state (Fig. 4c). The parameter β/χ (equation (1)), which is directly related to the extent of temperature rise, was consistently higher for liquid-filled CNTs (Fig. 4d). If we assume that the external heat transfer coefficient (h_{CNT-Si}) to the SiO_2 substrate remains invariant, estimated at 2,000 W m^2 K^{-1}, then k_a can be obtained by energy balance (Fig. 4b,e, and Supplementary Section 4). We find that on liquid water filling k_a decreases relative to the unfilled state by up to 500%. In this way, reversible phase changes of this type can toggle and control the heat flux, and form the basis of thermal diodes[49,50].

Conclusions

We measured the phase boundaries of confined water in isolated CNTs of various diameters, demonstrating a unique and extreme sensitivity to this parameter. Several of the reversible transitions are shown to be substantially higher than the values predicted by MD simulation, and highlight a number of new directions for the study of such phases. Our results enable the study and application of ice NTs at room temperature and above. We also report diameters that display melting transitions at room temperature, enabling new phase-change materials. The modulation of thermal conductivity with phase change in the interior of the CNTs enables the digital control of heat flux through these nanoconduits. Overall, these results underscore new opportunities for phase transitions of confined fluids inside CNTs.

Methods

Methods and any associated references are available in the online version of the paper.

Received 4 May 2015; accepted 17 October 2016; published online 28 November 2016

References

1. Shultz, M. J., Vu, T. H., Meyer, B. & Bisson, P. Water: a responsive small molecule. *Acc. Chem. Res.* **45,** 15–22 (2012).
2. Iijima, S. & Ichihashi, T. Single-shell carbon nanotubes of 1-nm diameter. *Nature* **363,** 603–605 (1993).
3. Koga, K., Gao, G. T., Tanaka, H. & Zeng, X. C. Formation of ordered ice nanotubes inside carbon nanotubes. *Nature* **412,** 802–805 (2001).
4. Hummer, G., Rasaiah, J. C. & Noworyta, J. P. Water conduction through the hydrophobic channel of a carbon nanotube. *Nature* **414,** 188–190 (2001).
5. Zhao, Y. *et al.* Individual water-filled single-walled carbon nanotubes as hydroelectric power converters. *Adv. Mater.* **20,** 1772–1776 (2008).
6. Fornasiero, F. *et al.* Ion exclusion by sub-2-nm carbon nanotube pores. *Proc. Natl Acad. Sci. USA* **105,** 17250–17255 (2008).
7. Walther, J. H., Ritos, K., Cruz-Chu, E. R., Megaridis, C. M. & Koumoutsakos, P. Barriers to superfast water transport in carbon nanotube membranes. *Nano Lett.* **13,** 1910–1914 (2013).
8. Noy, A. *et al.* Nanofluidics in carbon nanotubes. *Nano Today* **2,** 22–29 (2007).
9. Perez, M. Gibbs–Thomson effects in phase transformations. *Scr. Mater.* **52,** 709–712 (2005).
10. Christenson, H. K. Confinement effects on freezing and melting. *J. Phys. Condens. Matter.* **13,** R95–R133 (2001).
11. Maniwa, Y. *et al.* Phase transition in confined water inside carbon nanotubes. *J. Phys. Soc. Jpn* **71,** 2863–2866 (2002).
12. Takaiwa, D., Hatano, I., Koga, K. & Tanaka, H. Phase diagram of water in carbon nanotubes. *Proc. Natl Acad. Sci. USA* **105,** 39–43 (2008).
13. Bai, J., Wang, J. & Zeng, X. C. Multiwalled ice helixes and ice nanotubes. *Proc. Natl Acad. Sci. USA* **103,** 19664–19667 (2006).
14. Koga, K., Parra, R. D., Tanaka, H. & Zeng, X. C. Ice nanotube: what does the unit cell look like? *J. Chem. Phys.* **113,** 5037–5040 (2000).
15. Kyakuno, H. *et al.* Confined water inside single-walled carbon nanotubes: global phase diagram and effect of finite length. *J. Chem. Phys.* **134,** 244501 (2011).
16. Mann, D. J. & Halls, M. D. Water alignment and proton conduction inside carbon nanotubes. *Phys. Rev. Lett.* **90,** 195503 (2003).
17. Maniwa, Y. *et al.* Ordered water inside carbon nanotubes: formation of pentagonal to octagonal ice-nanotubes. *Chem. Phys. Lett.* **401,** 534–538 (2005).
18. Mikami, F., Matsuda, K., Kataura, H. & Maniwa, Y. Dielectric properties of water inside single-walled carbon nanotubes. *ACS Nano* **3,** 1279–1287 (2009).
19. Maniwa, Y. *et al.* Water-filled single-wall carbon nanotubes as molecular nanovalves. *Nat. Mater.* **6,** 135–141 (2007).
20. Shiomi, J., Kimura, T. & Maruyama, S. Molecular dynamics of ice-nanotube formation inside carbon nanotubes. *J. Phys. Chem. C* **111,** 12188–12193 (2007).
21. Ghosh, S., Ramanathan, K. V. & Sood, A. K. Water at nanoscale confined in single-walled carbon nanotubes studied by NMR. *Europhys. Lett.* **65,** 678–684 (2004).
22. Luo, C., Fa, W., Zhou, J., Dong, J. & Zeng, X. C. Ferroelectric ordering in ice nanotubes confined in carbon nanotubes. *Nano Lett.* **8,** 2607–2612 (2008).
23. Pascal, T. A., Goddard, W. A. & Jung, Y. Entropy and the driving force for the filling of carbon nanotubes with water. *Proc. Natl Acad. Sci. USA* **108,** 11794–11798 (2011).
24. Striolo, A., Chialvo, A. A., Gubbins, K. E. & Cummings, P. T. Water in carbon nanotubes: adsorption isotherms and thermodynamic properties from molecular simulation. *J. Chem. Phys.* **122,** 234712 (2005).
25. Ghosh, S., Sood, A. K. & Kumar, N. Carbon nanotube flow sensors. *Science* **299,** 1042–1044 (2003).
26. Lee, C. Y., Choi, W., Han, J.-H. & Strano, M. S. Coherence resonance in a single-walled carbon nanotube ion channel. *Science* **329,** 1320–1324 (2010).
27. Holt, J. K. *et al.* Fast mass transport through sub-2-nanometer carbon nanotubes. *Science* **312,** 1034–1037 (2006).
28. Corry, B. Designing carbon nanotube membranes for efficient water desalination. *J. Phys. Chem. B* **112,** 1427–1434 (2008).
29. Striolo, A. The mechanism of water diffusion in narrow carbon nanotubes. *Nano Lett.* **6,** 633–639 (2006).
30. Cabeza, L. F., Mehling, H., Hiebler, S. & Ziegler, F. Heat transfer enhancement in water when used as PCM in thermal energy storage. *Appl. Therm. Eng.* **22,** 1141–1151 (2002).
31. Thomas, M. & Corry, B. Thermostat choice significantly influences water flow rates in molecular dynamics studies of carbon nanotubes. *Microfluid. Nanofluid.* **18,** 41–47 (2015).
32. Werder, T., Walther, J. H., Jaffe, R. L., Halicioglu, T. & Koumoutsakos, P. On the water–carbon interaction for use in molecular dynamics simulations of graphite and carbon nanotubes. *J. Phys. Chem. B* **107,** 1345–1352 (2003).
33. Choi, W., Lee, C. Y., Ham, M.-H., Shimizu, S. & Strano, M. S. Dynamics of simultaneous, single ion transport through two single-walled carbon nanotubes: observation of a three-state system. *J. Am. Chem. Soc.* **133,** 203–205 (2011).
34. Choi, W. *et al.* Diameter-dependent ion transport through the interior of isolated single-walled carbon nanotubes. *Nat. Commun.* **4,** 2397 (2013).
35. Jorio, A. *et al.* Structural (*n,m*) determination of isolated single-wall carbon nanotubes by resonant Raman scattering. *Phys. Rev. Lett.* **86,** 1118–1121 (2001).
36. Jorio, A. *et al.* G-band resonant Raman study of 62 isolated single-wall carbon nanotubes. *Phys. Rev. B* **65,** 23–27 (2002).
37. Li, F. *et al.* Identification of the constituents of double-walled carbon nanotubes using Raman spectra taken with different laser-excitation energies. *J. Mater. Res.* **18,** 1251–1258 (2003).
38. Cambré, S., Schoeters, B., Luyckx, S., Goovaerts, E. & Wenseleers, W. Experimental observation of single-file water filling of thin single-wall carbon nanotubes down to chiral index (5,3). *Phys. Rev. Lett.* **104,** 207401 (2010).
39. Wenseleers, W., Cambré, S., Čulin, J., Bouwen, A. & Goovaerts, E. Effect of water filling on the electronic and vibrational resonances of carbon nanotubes: characterizing tube opening by Raman spectroscopy. *Adv. Mater.* **19,** 2274–2278 (2007).
40. Longhurst, M. J. & Quirke, N. The environmental effect on the radial breathing mode of carbon nanotubes. II. Shell model approximation for internally and externally adsorbed fluids. *J. Chem. Phys.* **125,** 184705 (2006).
41. Zhang, Y., Son, H., Zhang, J., Kong, J. & Liu, Z. Laser-heating effect on Raman spectra of individual suspended single-walled carbon nanotubes. *J. Phys. Chem. C* **111,** 1988–1992 (2007).
42. Zhang, Y., Xie, L., Zhang, J., Wu, Z. & Liu, Z. Temperature coefficients of Raman frequency of individual single-walled carbon nanotubes. *J. Phys. Chem. C* **111,** 14031–14034 (2007).
43. Huang, F. *et al.* Temperature dependence of the Raman spectra of carbon nanotubes. *J. Appl. Phys.* **76,** 2053–2055 (2000).
44. Wang, C. Y., Ru, C. Q. & Mioduchowski, A. Free vibration of multiwall carbon nanotubes. *J. Appl. Phys.* **97,** 114323 (2005).
45. Efron, B. & Tibshirani, R. Bootstrap methods for standard errors, confidence intervals, and other measures of statistical accuracy. *Stat. Sci.* **1,** 54–75 (1986).
46. Chiashi, S. *et al.* Water encapsulation control in individual single-walled carbon nanotubes by laser irradiation. *J. Phys. Chem. Lett.* **5,** 408–412 (2014).
47. Sliwinska-Bartkowiak, M., Jazdzewska, M., Huang, L. L. & Gubbins, K. E. Melting behavior of water in cylindrical pores: carbon nanotubes and silica glasses. *Phys. Chem. Chem. Phys.* **10,** 4909–4919 (2008).
48. Radhakrishnan, R., Gubbins, K. E. & Sliwinska-Bartkowiak, M. Global phase diagrams for freezing in porous media. *J. Chem. Phys.* **116,** 1147–1155 (2002).
49. Chang, C. W., Okawa, D., Majumdar, A. & Zettl, A. Solid-state thermal rectifier. *Science* **314,** 1121–1124 (2006).
50. Takahashi, K., Inoue, M. & Ito, Y. Defective carbon nanotube for use as a thermal rectifier. *Jpn J. Appl. Phys.* **49,** 02BD12 (2010).

Acknowledgements

This work was supported in part by the U. S. Army Research Laboratory and the U. S. Army Research Office through the Institute for Soldier Nanotechnologies, under contract number W911NF-13-D-0001. We acknowledge support from the Shell-MIT-EI Energy Research Fund as well. We also acknowledge support from the National Science Foundation under Grant Number 1306529.

Author contributions

K.V.A, S.S. and M.S.S. conceived and designed the experiments. K.V.A., S.S., L.W.D. and D.K. performed the experiments, analyzed the data, and contributed materials/analysis tools. K.V.A. and M.S.S. wrote the paper. All authors commented on the manuscript.

Additional information

Supplementary information is available in the online version of the paper. Reprints and permissions information is available online at www.nature.com/reprints. Correspondence and requests for materials should be addressed to M.S.S.

Competing financial interests

The authors declare no competing financial interests.

Methods

We synthesized horizontally aligned ultralong CNTs on Si wafers by the CVD process described in our previous report[34]. Briefly, a thin line of Fe catalyst was patterned on an edge of the wafer (Fig. 1a,(i)), and CNTs were grown in the presence of CH_4 (carbon source) and H_2 at 970 °C at 1 atmospheric pressure inside a horizontal quartz tube furnace. As-synthesized CNTs, with closed ends, were mapped by SEM (JEOL 6010LA) to pinpoint their location on the Si wafer.

Mapped CNTs were searched by microRaman spectroscopy (Horiba LabRAM, 532 nm, 2.33 eV, 8 mW, grating 1800, ×100 objective). The data acquisition was carried out using LabSpec (version 5). The spectrometer was calibrated using cyclohexane at 801.8 cm^{-1}. The CNTs were identified by scanning an approximate area (from SEM mapping), and maximizing the *G* peak height. *G* peak height would be maximized when the CNT falls at the centre of the laser spot. The 100–1,800 cm^{-1} wavenumber range was scanned (accumulation 2×, exposure time of 10 s) to obtain the RBM and the *G* peaks. CNT diameter and chirality were obtained using the RBM peak position ($d = 248/\mathrm{RBM}$)[35,37] and the shape of the *G* peak[36].

To study temperature-dependent variations in the RBM and the *G* peak positions, the Si wafer containing aligned CNTs was placed on the variable-temperature stage (Linkam Scientific, THMS600 stage with the T95 controller and the LNP95 liquid nitrogen pump). The THMS600 stage consisted of 22 mm diameter silver heating/cooling block for achieving high thermal conductivity for quick temperature stabilization.

To calculate X for the empty tubes, which is $(\partial G/\partial T)P_{\mathrm{laser}} \sim 0$, the temperature of the stage was varied and using a low laser power (0.08 mW), and the position of the *G* peak was recorded as a function of the temperature (accumulation 2×, exposure time 120–300 s depending on the signal-to-noise ratio). Higher exposure times were not possible due to stage drifting issues. χ was calculated as the slope of the curve (*G* peak position as a function of the temperature).

To calculate β for the empty tubes, which is $(\partial G/\partial P_{\mathrm{laser}})_{T=20^{\circ}\mathrm{C}}$, the position of the *G* peak was measured as a function of the laser power (0.08–8 mW) at 20 °C. The laser power was varied using a variable, continuous neutral density filter (Thorlabs), which was calibrated using a power meter before each experiment.

Typically, 1 tube per Si wafer met the following criteria:

(1) The tube should run straight throughout the length of the Si wafer without kinks and turns.
(2) There should be no change in the chirality of the tube along the length.
(3) No defects (indicated by the *D* peak) should be present. No discernable *D* peak was recorded for the tubes studied here.

Slight changes in the *G* peak position were observed at different lengths of the tube. This can be attributed to the varying doping as a function of substrate position. To circumvent this issue, the entire phase transition experiment (data in Supplementary Fig. 3, and Fig. 2a–b) was carried out at a single spot. The spots for measurements of χ and β were not necessarily same as those where the phase transition experiments were carried out. However, all of the data for χ and β were generated at the same spot. One can assume that the slope of *G* peak position with respect to the temperature (χ) and the laser power does not change significantly with the location on the Si wafer (χ and β are intrinsic properties of the tube).

In post-analysis of the empty CNT, the middle section of the tube (typically 1–10 mm) was covered by a homemade PDMS mask, and the exposed ends of the device were etched in an air plasma (Harrick Plasma) for 3 min, thereby opening the tube from both the ends. The mask was carefully removed, and PDMS reservoirs were established on both ends of the device.

The device with the water-filled reservoir was placed on the heating stage, and microRaman spectroscopy was repeated to obtain X and β for the filled tube. Care was taken to maintain the water in the reservoir at the elevated temperatures. Temperature-dependent scans were collected to obtain the phase behaviour of water (Supplementary Fig. 3). As mentioned before, all of the data were collected at the same spot (within 1 μm length, laser spot size 5 μm).

The RBM and *G* peak intensities reduced for the filled CNTs compared with those from the empty CNTs (for example, refer to the dynamic filling experiment in Fig. 1b). Moreover, stage drift was significant when the stage was heated or cooled, often leading to low signal-to-noise ratio, or a complete loss of the CNT signal. In such cases, multiple spectra were taken after refocusing/adjusting the sample. This limited exposure time to 120 s. A signal-to-noise ratio threshold of two was used as a criterion to accept or reject the data.

Analysis of Raman spectrum. To analyse the Raman data, the background was subtracted from the Raman spectrum. Peak fitting was carried out using a least-squares curve fitting tool (MATLAB, lsqnonlin) and fitting the peak to a Lorentzian curve, which yielded the peak position, area and FWHM. The corresponding errors were also obtained. For Supplementary Fig. 3, the RBM peaks were normalized.

For determination of the phase transition temperature by the finite-width Heaviside fitting (Fig. 2b), RBM peak positions recorded at the same temperature, in the same heating/cooling cycle, and with a poor signal-to-noise ratios were averaged. The only exceptions to this rule were RBM peaks with a shoulder. In these cases, the peaks were deconvoluted to two peaks (liquid and vapour, solid and liquid), and were represented in the Fig. 2b with circular markers with a size proportional to the peak area. The weights of all of the data points in the Heaviside fitting were 1. The fitting for deconvoluted data points included fractional weights proportional to the peak area. The phase transition data was fitted with the finite-width double Heaviside function (equation (4)). Bootstrap sampling[45] was employed to obtain a fit (Fig. 2b) due to the lack of a large data set.

$$y = \frac{Y_A + Y_c}{2} + \left|\frac{Y_A - Y_B}{2}\right| \mathrm{erf}\left(\frac{T1 - T}{s1}\right) + \left|\frac{Y_B - Y_C}{2}\right| \mathrm{erf}\left(\frac{T2 - T}{s2}\right) \quad (4)$$

where $T1$ and $T2$ are solid-liquid and liquid-vapor phase transition temperatures, respectively. Y_A, Y_B and Y_C are the fitted RBM peak positions corresponding to the solid, liquid and the dry states, respectively. $s1$ and $s2$ are the 2 slopes of finite-width double Heaviside functions. T and Y represent the temperature and RBM peak position of the fitted curve, respectively.